SUPPORTING INFORMATION

Modulating Photoelectrochemical Water-Splitting Activity by Charge-Storage Capacity of Electrocatalysts

Yawen Dai,[†,‡,§] Ping Cheng,[†,⊥,§] Guancai Xie,[†,‡,§] Chengcheng Li,[‖] Muhammad Zain Akram,[†,‡] Beidou Guo,[†,‡] Rajender Boddula,[†] Xinghua Shi,[†,‡,] Jinlong Gong,[‖,*] and Jian Ru Gong[†,*]*

[†]Chinese Academy of Sciences (CAS) Center for Excellence in Nanoscience, CAS Key Laboratory of Nanosystem and Hierarchy Fabrication, National Center for Nanoscience and Technology, Beijing 100190, China

[‡]University of Chinese Academy of Sciences, Beijing 100049, China

[⊥]College of Science, University of Shanghai for Science and Technology, Shanghai 200093, China

[‖]Tianjin University, Tianjin 300072, China

* Corresponding author: gongjr@nanoctr.cn (J.R.G.); jlgong@tju.edu.cn (J.G.); shixh@nanoctr.cn (X.S.)
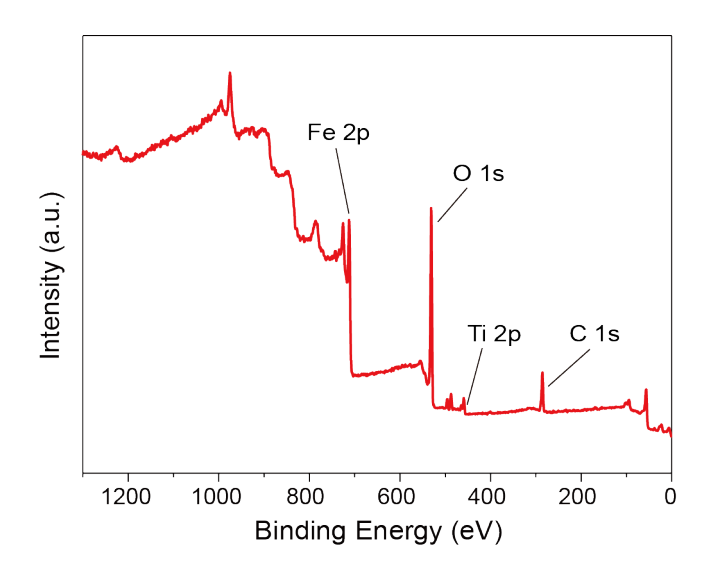
§ These authors contributed equally.

Figure S1. XPS survey spectrum of the α-Fe$_2$O$_3$ photoanode.
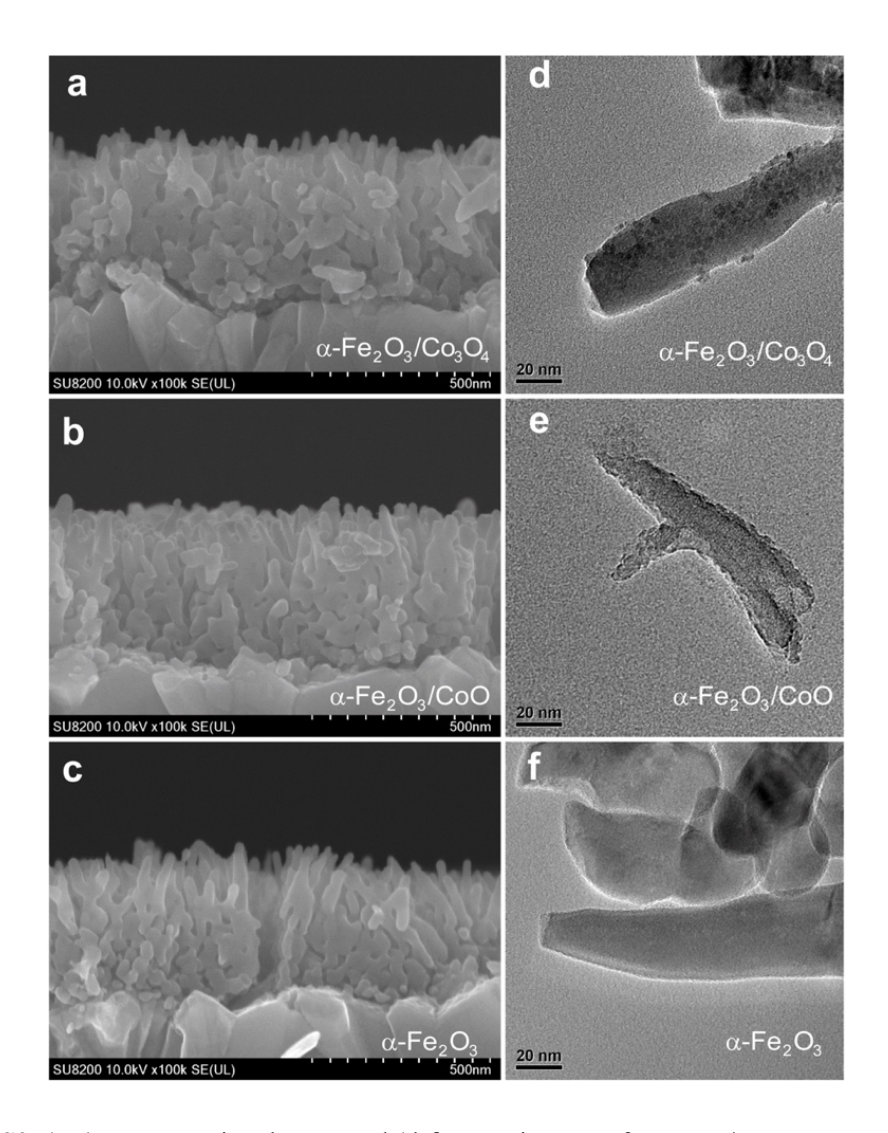
Figure S2. (a-c) Cross-sectional SEM and (d-f) TEM images of α-Fe$_2$O$_3$/Co$_3$O$_4$, α-Fe$_2$O$_3$/CoO, and α-Fe$_2$O$_3$.

Since both Co$_3$O$_4$ and CoO nanoparticles are spin coated on α-Fe$_2$O$_3$ with irregularly attached interfaces, no well-lattice-matched interfaces can be obtained regardless of the lattice constants. Therefore, the degree of lattice-mismatch of the α-Fe$_2$O$_3$-Co$_3$O$_4$ and the α-Fe$_2$O$_3$-CoO interfaces can be regarded similar, and thus the interface defects should not be the determinant reason for the PEC OER activity difference.
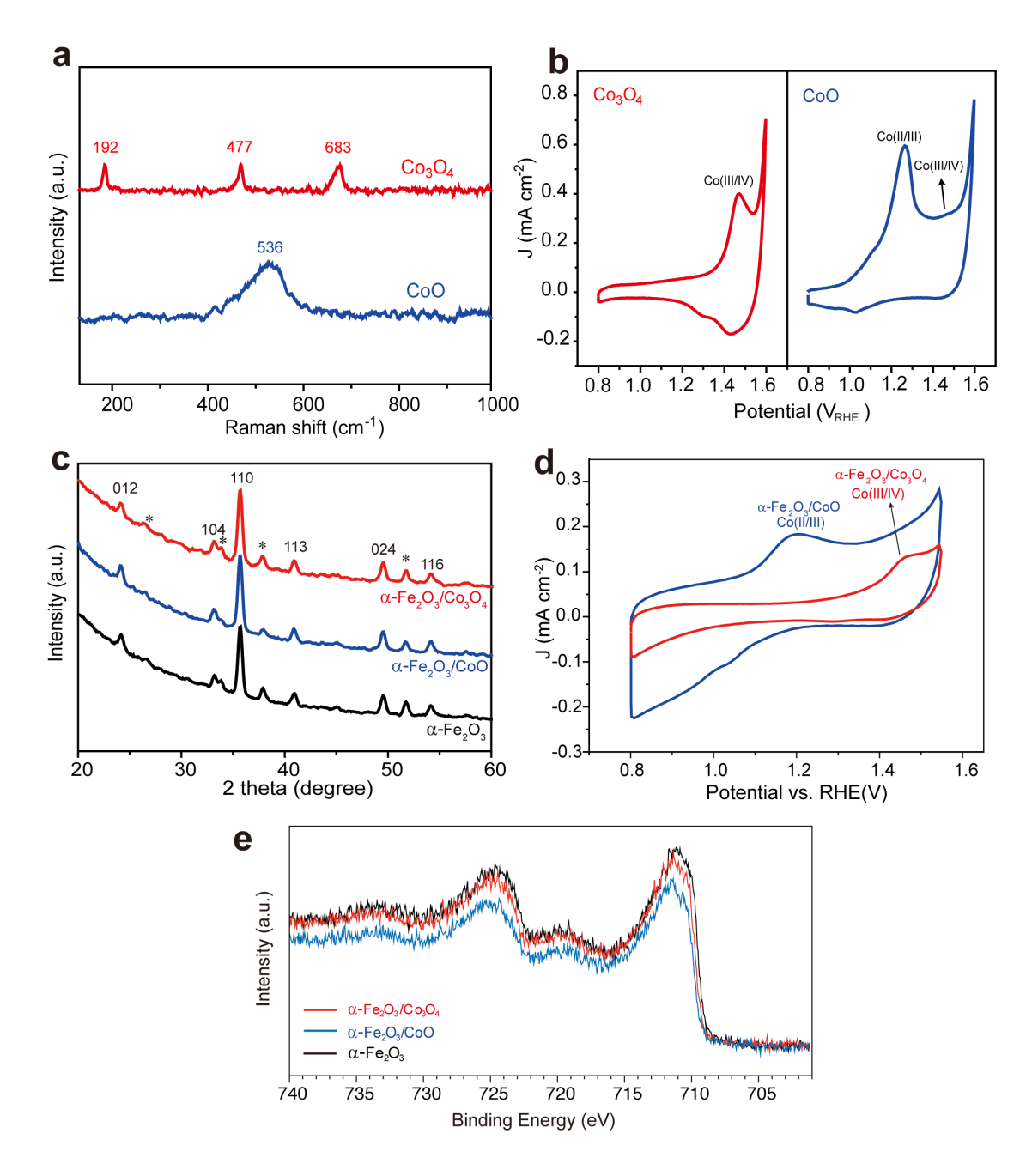
Figure S3. (a) Raman spectra and (b) cyclic voltammetry plots of Co_3O_4 and CoO coated FTO. (c) XRD patterns of α-Fe_2O_3/Co_3O_4, α-Fe_2O_3/CoO, and α-Fe_2O_3. *labels SnO_2. (d) Dark CV curves of α-Fe_2O_3/Co_3O_4 and α-Fe_2O_3/CoO. (e) XPS Fe 2p spectra of α-Fe_2O_3/Co_3O_4, α-Fe_2O_3/CoO, and α-Fe_2O_3.

In the Raman spectra (Figure S3a), the single broad peak at 536 cm^{-1} is assigned to rock salt CoO, while the relatively sharp peaks located at 192, 477, and 683 cm^{-1} are assigned to spinel Co_3O_4.[1] The oxidation peaks in CV plots (Figure S3b) at 1.47 V_{RHE} for Co_3O_4 and 1.26 V_{RHE} for CoO are assigned to the Co (III)/Co (IV) and Co (II)/Co (III) couples, respectively, indicating the dominant valence states of Co (III) in Co_3O_4 and Co (II) in CoO.[2-3] The CV curves

are used to demonstrate the original chemical states in the two catalysts instead of detecting OER intermediates. The Co (III)/Co (IV) oxidation peak in CoO is weak because of the original chemical state of Co (II), which is a commonly observed phenomenon as in other reports,[2,4] but it also reaches Co (IV) when catalysing OER as demonstrated by the in-situ characterization by other researchers.[4]

We have also presented CV diagrams (Figure S3d) and XPS Fe 2p spectra (Figure S3e) of α-Fe$_2$O$_3$/Co$_3$O$_4$ and the α-Fe$_2$O$_3$/CoO. After the deposition of electrocatalysts, feature redox peaks of Co(II/III) in α-Fe$_2$O$_3$/CoO and Co(III/IV) in α-Fe$_2$O$_3$/Co$_3$O$_4$ are both observed in their corresponding CV diagrams (Figure S3d), suggesting the decent coverage of the electrocatalysts on the surface of the nano-hematite. Besides, the XPS Fe 2p intensity decreases compared to that of bare hematite (Figure S3e), indicating the successful deposition of the electrocatalysts. These results suggest the interface between hematite and electrocatalyst should play important roles in their PEC activity although the distribution of electrocatalysts on the hematite is not very uniform.
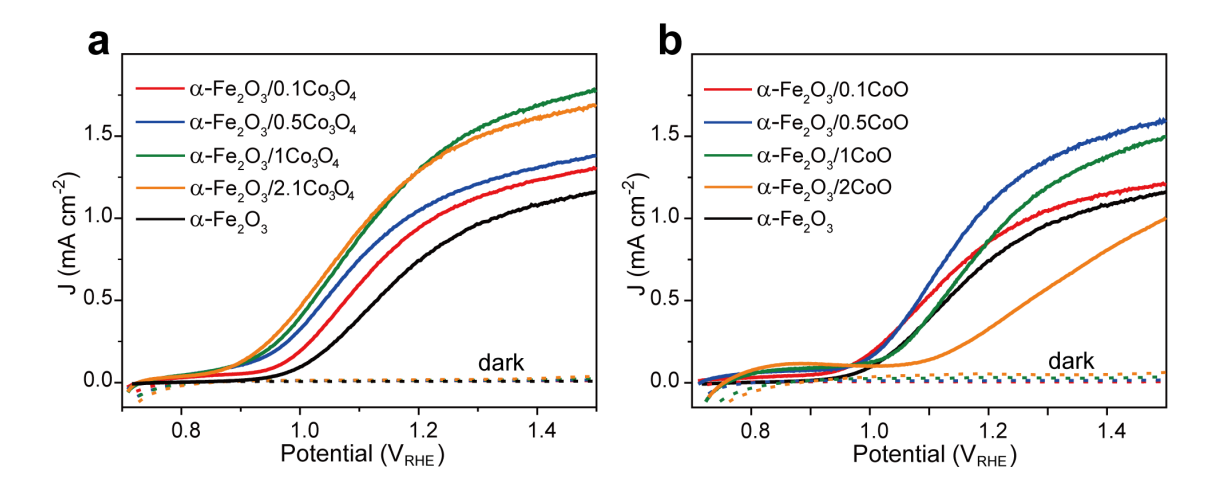
Figure S4. Photocurrent densities of α-Fe$_2$O$_3$ coated by (a) Co$_3$O$_4$ and (b) CoO with different loading amount of the ECs. α-Fe$_2$O$_3$/xEC indicates the α-Fe$_2$O$_3$ spin coated by x mg mL^{-1} EC dispersion. Dashed lines represent the corresponding dark current densities.

The onset potentials of all the Co$_3$O$_4$ coated α-Fe$_2$O$_3$ photoandes are more cathodic compared to that of the bare one, and increasing the Co$_3$O$_4$ loading amount leads to increasingly more cathodically shifted onset potentials. α-Fe$_2$O$_3$/0.1CoO shows a little more cathodic onset potential than the bare α-Fe$_2$O$_3$, whereas increasing the CoO loading amount gradually leads to anodically shifted onset potentials. In order to highlight the opposite effect of Co$_3$O$_4$ and CoO, α-Fe$_2$O$_3$ photoanodes coated by 2.1 mg mL^{-1} Co$_3$O$_4$ and 2 mg mL^{-1} CoO dispersion (both contain 1.5 mg mL^{-1} Co element) are chosen as the model samples for further in-depth investigation.

Additionally, it can be noticed that a small loading amount of 0.5 mg mL^{-1} CoO is also working decently, which is due to its relatively low hole storage capacity thus inducing relatively low interfacial recombination. Therefore, the methods of tuning ECs' hole storage capacity include tuning the loading amount, valence states as explained in the main text, or elemental constituents as indicated by the experiments from Hamann et al.[5] Regardless of the tuning method used, we should be aware that in essence it is the ECs' hole storage capacity that plays a key role in balancing the competition between interfacial charge transfer and recombination, thus dominating the PEC OER activity of an EC modified photoanode.
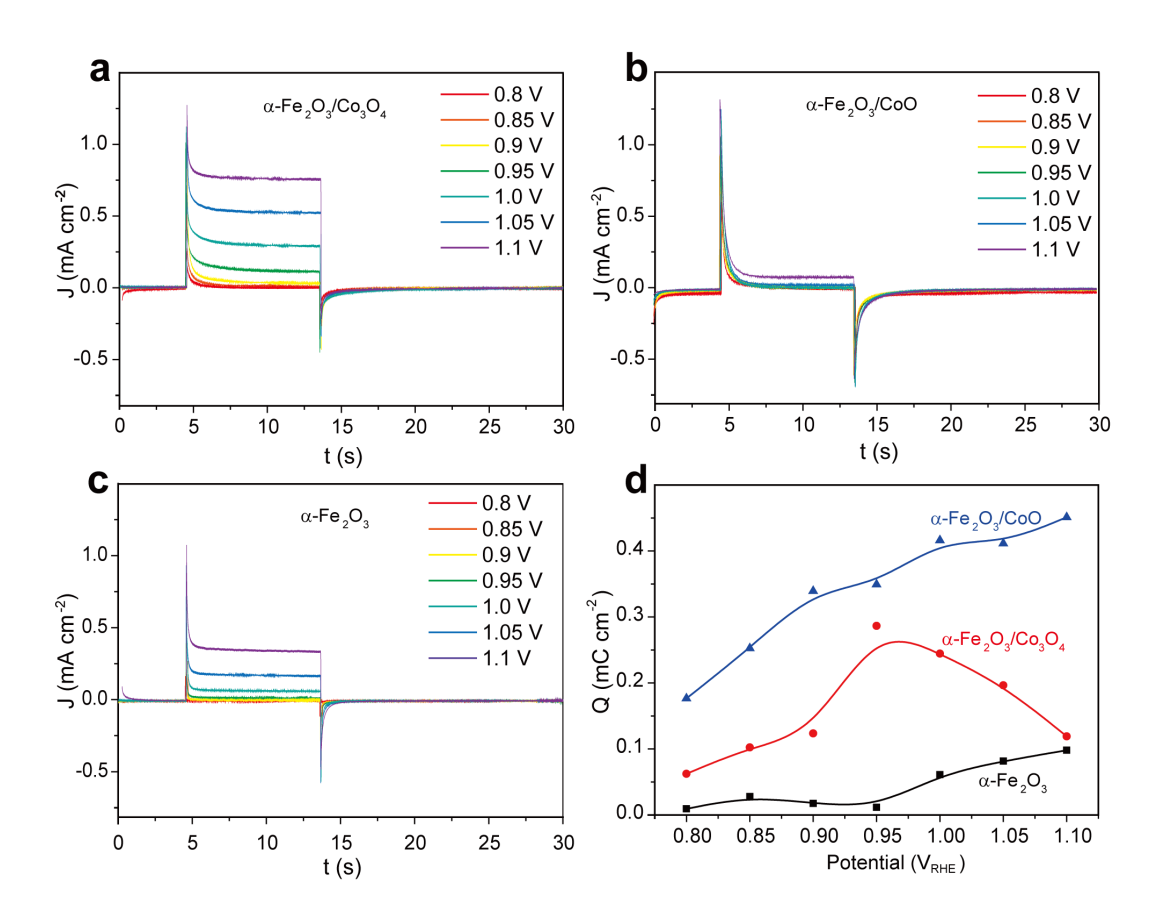
Figure S5. Chopped light chronoamperometry measurements of (a) α-Fe₂O₃/Co₃O₄, (b) α-Fe₂O₃/CoO, and (c) α-Fe₂O₃ at 0.8-1.1V$_{RHE}$, (d) the hole accumulation density calculated by integrating the cathodic transient photocurrent region.
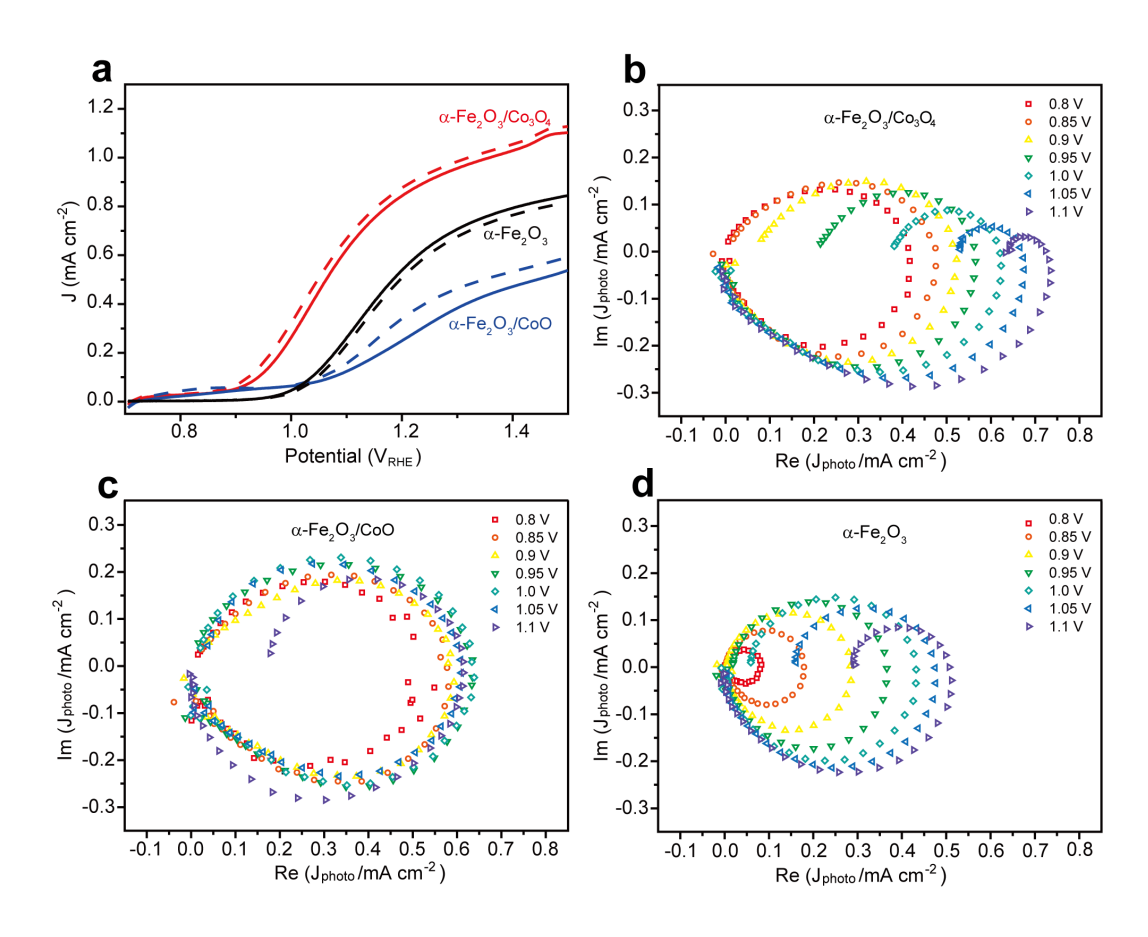
Figure S6. (a) J-V curves under 100 mW cm^{-2} white LED before (solid lines) and after (dashed lines) the IMPS test. Full IMPS complex plots of (b) α-Fe$_2$O$_3$/Co$_3$O$_4$, (c) α-Fe$_2$O$_3$/CoO, and (d) α-Fe$_2$O$_3$ at 0.8-1.1 V$_{RHE}$.
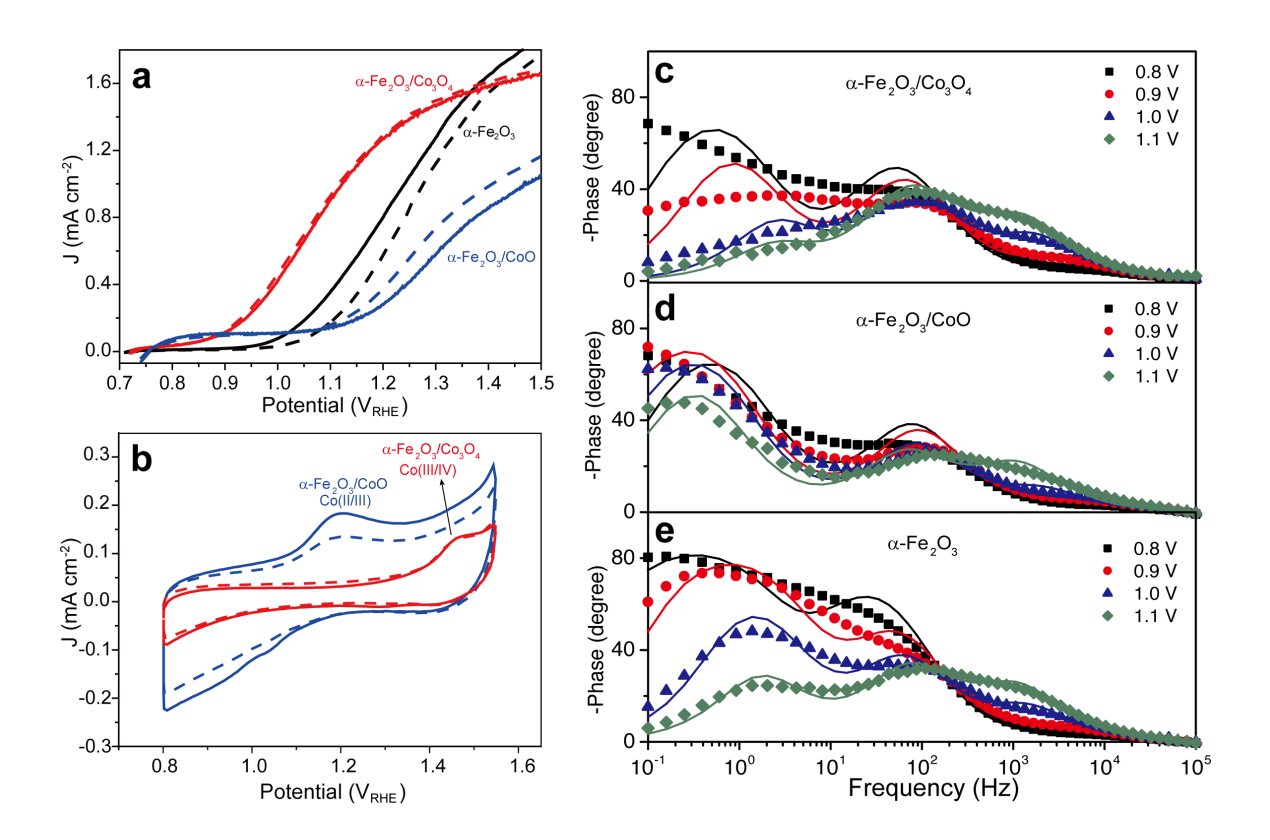
Figure S7. (a) J-V curves under 1 sun irradiation of α-Fe₂O₃/Co₃O₄, α-Fe₂O₃/CoO, and α-Fe₂O₃, (b) dark CV curves of α-Fe₂O₃/Co₃O₄ and α-Fe₂O₃/CoO before (solid lines) and after (dashed lines) the PEIS test. Bode plots (dotted lines) and the corresponding fitted (solid) lines for (c) α-Fe₂O₃/Co₃O₄, (d) α-Fe₂O₃/CoO, and (e) α-Fe₂O₃.

The equivalent circuit used to fit the PEIS data consists of a solution resistance (R_s), a resistance ($R_{FTO-bulk}$) and a capacitance ($C_{FTO-bulk}$) in parallel to simulate the FTO-α-Fe₂O₃ interface, a capacitance of bulk α-Fe₂O₃ (C_{bulk}), and the other capacitances and resistances (R_{trap}, R_{ct}, C_{surf}) that have been explained in the main text.
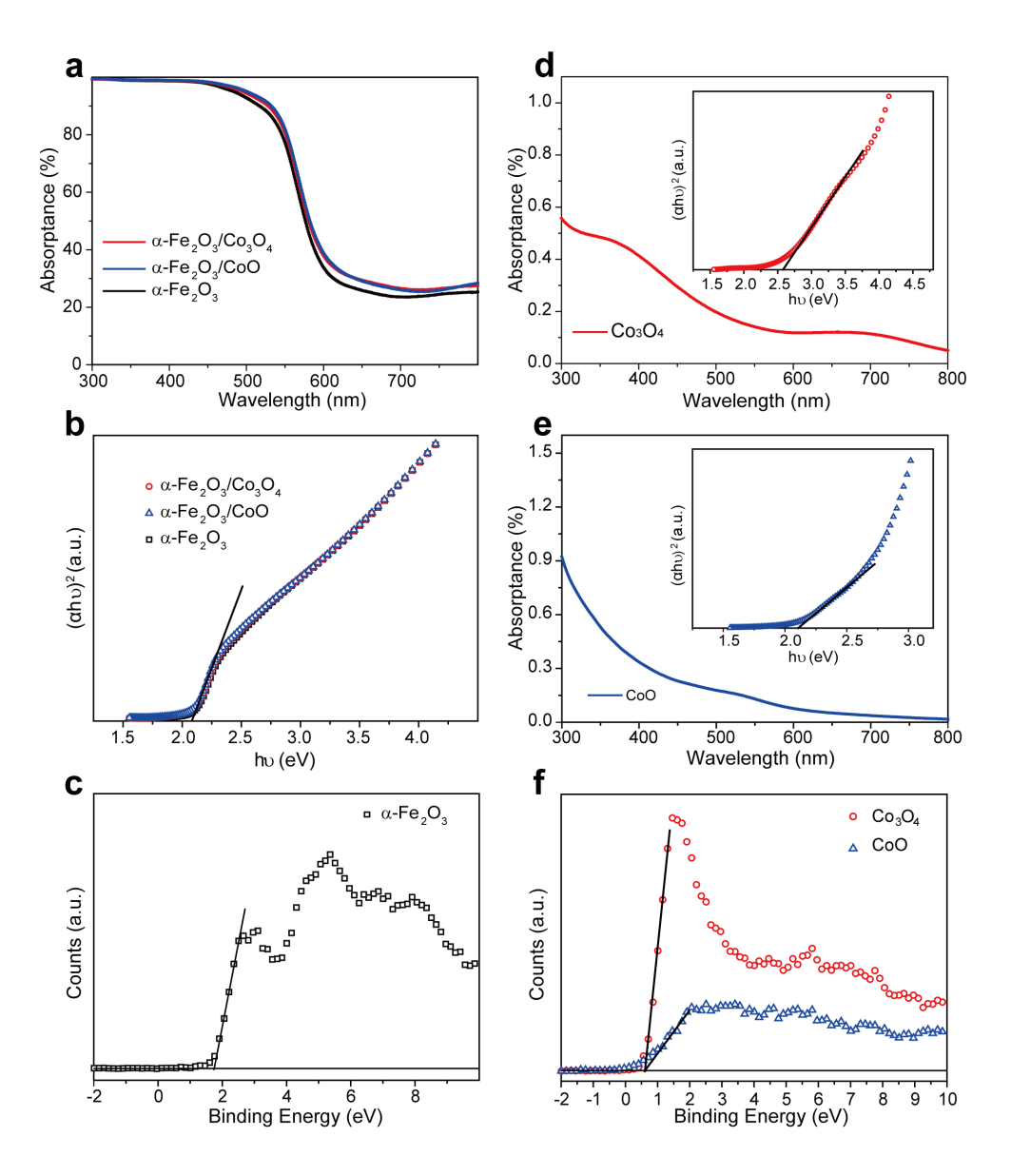
Figure S8. (a) UV-visible absorptance spectra and (b) the corresponding Tauc plots of α-Fe$_2$O$_3$/Co$_3$O$_4$, α-Fe$_2$O$_3$/CoO, and α-Fe$_2$O$_3$; (c) the valence band region of the XPS spectrum of α-Fe$_2$O$_3$. (d) UV-visible absorptance spectra, (e) the corresponding Tauc plots, and (f) the valence band region of the XPS spectra of Co$_3$O$_4$ and CoO.

The conductivity types of α-Fe$_2$O$_3$, Co$_3$O$_4$, and CoO were confirmed by combining the bandgap measurements with the XPS spectra. All α-Fe$_2$O$_3$ films with and without EC coating have a bandgap value of 2.1 eV as indicated by the UV-visible absorptance spectra (Figure S8a) and the corresponding Tauc plots (Figure S8b). The valence band region of the XPS spectrum of α-Fe$_2$O$_3$ (Figure S8c) shows that the distance between the position of valence band (E$_{VB}$) and the Fermi level (E$_F$) is 1.7 eV, and thus the distance between E$_F$ and the position of the conduction band (E$_{CB}$) is 0.4 eV. Therefore, the closer E$_F$-E$_{CB}$ distance than the E$_{VB}$-E$_F$ distance indicates the n-type conductivity of α-Fe$_2$O$_3$. Bandgap val-

ues of 2.6 eV for Co_3O_4 and 2.1 eV for CoO are obtained from their UV-visible absorptance spectra (Figure S8d) and the corresponding Tauc plots (Figure S8e). The valence band region of the XPS spectra (Figure S8f) shows that the E_{VB}-E_F distance is 0.6 eV for both Co_3O_4 and CoO, and thus the E_F-E_{CB} distances are 2.0 eV for Co_3O_4 and 1.5 eV for CoO. Therefore, the closer E_{VB}-E_F distance than the E_F-E_{CB} distance indicates that both Co_3O_4 and CoO are p-type semi-conductors.[6] The above conductivity type analysis indicates that both ECs can form p-n junctions with α-Fe_2O_3.
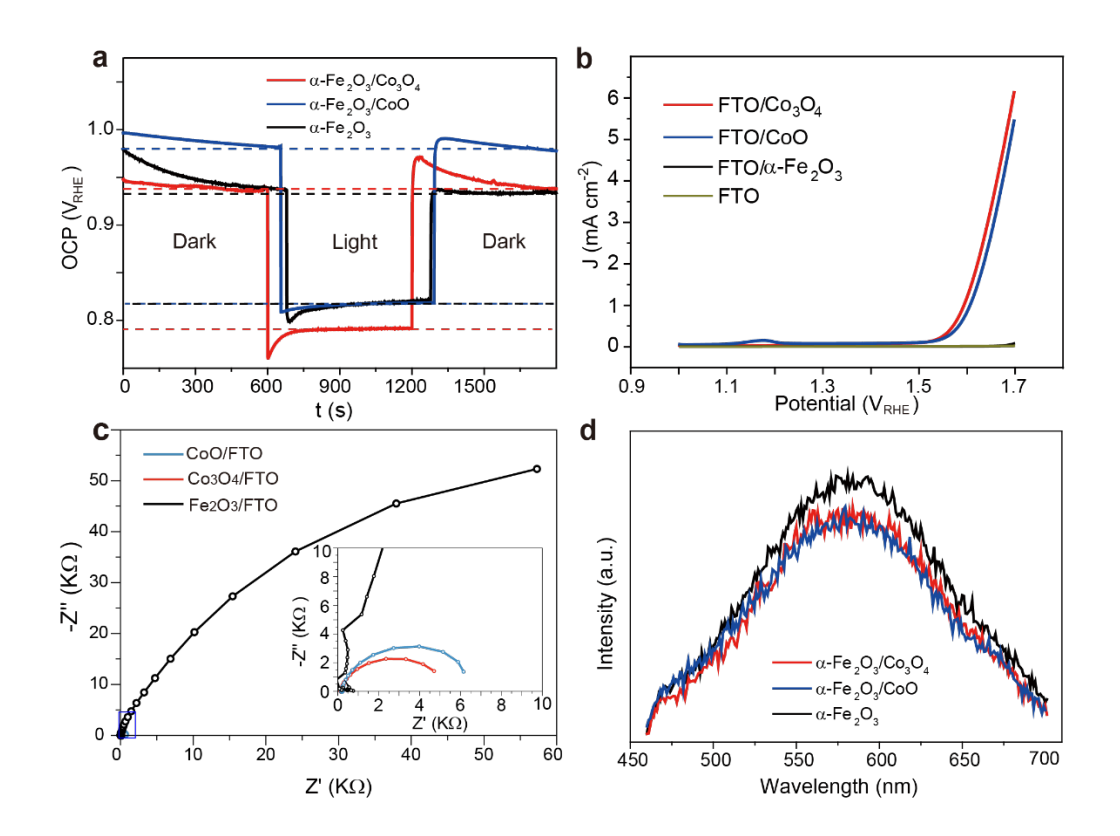
Figure S9. (a) OCP measurements of α-Fe$_2$O$_3$/Co$_3$O$_4$, α-Fe$_2$O$_3$/CoO, and α-Fe$_2$O$_3$. (b) Dark J-V curves of Co$_3$O$_4$/FTO, CoO/FTO, α-Fe$_2$O$_3$/FTO, and the bare FTO. (c) EIS Nyquist plots of Co3O4/FTO, CoO/FTO, and α -Fe$_2$O$_3$/FTO measured at 1.57 V$_{RHE}$. Inset is the zoom-in view of the blue rectangle zone. (d) Photoluminescence emission spectra of α-Fe$_2$O$_3$/Co$_3$O$_4$, α-Fe$_2$O$_3$/CoO and α-Fe$_2$O$_3$.

The open-circuit potentials (OCPs) of all three photoanodes were measured (Figure S9a), and the difference between the OCPs measured in the dark and under illumination of a photoanode is regarded as the photovoltage. The photovoltage of α-Fe$_2$O$_3$ (114 mV) increases after coating the ECs (147 mV for α-Fe$_2$O$_3$/Co$_3$O$_4$ and 160 mV for α-Fe$_2$O$_3$/CoO). The increased photovoltages of the EC-coated photoanodes compared to that of the bare one (Figure S9a) can be attributed to the passivation of surface states, or the formation of p-n junctions between α-Fe$_2$O$_3$ and the ECs as inferred from the conductivity type analysis (Figure S8a-S8f). Figure S9b shows that the overpotentials at 1 mA cm^{-2} for Co$_3$O$_4$ and CoO are 360 and 370 mV, respectively, and the small difference indicates that the two ECs are similarly active for the OER. Furthermore, only one semi-circle arc corresponding to the EC-electrolyte interfacial charge transfer resistance is shown for both electrodes as well as bare hematite (Figure S9c). Only one semi-circle arc corresponding to the EC-electrolyte interfacial charge transfer resistance is shown for both electrodes as well as bare hematite. Both

ECs possess significantly smaller arc than bare hematite, indicating their excellent electrocatalytic OER activity in comparison with bare hematite. Moreover, in accordance with the potential sweep curves in Figure S9b, the Co_3O_4/FTO electrode also shows a similar arc with the CoO/FTO, revealing their similar reaction kinetics for OER. Therefore, the electrocatalytic OER activities of CoO and Co_3O_4 is also not the determinant reason for the PEC OER activity difference.
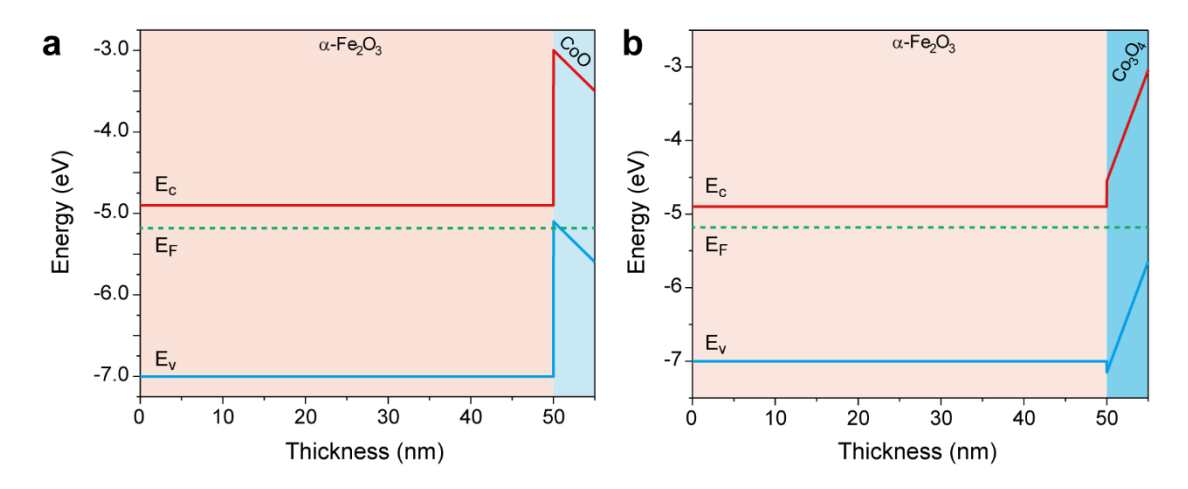
Figure S10. Simulated band diagrams of the (a) α-Fe$_2$O$_3$/CoO and (b) α-Fe$_2$O$_3$/Co$_3$O$_4$ heterojunctions using the AFORS-HET program. E$_c$, E$_v$, and E$_F$ represent for conduction band minimum, valence band maximum, and Fermi level, respectively.

Figure S10 shows the simulated band diagrams of the α-Fe$_2$O$_3$/Co$_3$O$_4$ and α-Fe$_2$O$_3$/CoO heterojunctions using the AFORS-HET program[7] based on the parameters in Table S1. As can be seen from Figure S10, there is no significant band bending observed at the interface of both heterojunctions, in which the band tilt in CoO and Co$_3$O$_4$ may be due to their small size that cannot be correctly handled by this program.

Table S1. Parameters and the corresponding values used in the simulation by the AFORS-HET program.

| Material	α-Fe$_2$O$_3$	CoO	Co$_3$O$_4$
Film thickness (nm)	50	5	5
dielectric constant-dk	80[8]	12.9[9]	13[10]
Electron affinity-chi (eV)	4.9[11]	3[12]	4.55[10]
Band gap-E$_g$ (eV)	2.1	2.1	2.6
Effective conduction band density-N$_c$ (cm^{-3})	5.3E20[13]	1E19	8.9E19[14]
Effective valence band density-N$_v$ (cm^{-3})	2E19[13]	1E19	6.3E19[14]
Effective electron mobility-μ_n (cm^{-2} V^{-1} S^{-1})	4.5[13]	0.3[15]	1[16]
Effective hole mobility-μ_p (cm^{-2} V^{-1} S^{-1})	1.5[13]	0.3[15]	1[16]
Doping concentration acceptors-N$_a$ (cm^{-3})	0	1E12	1E12
Doping concentration donors-N$_d$ (cm^{-3})	1E16	0	0
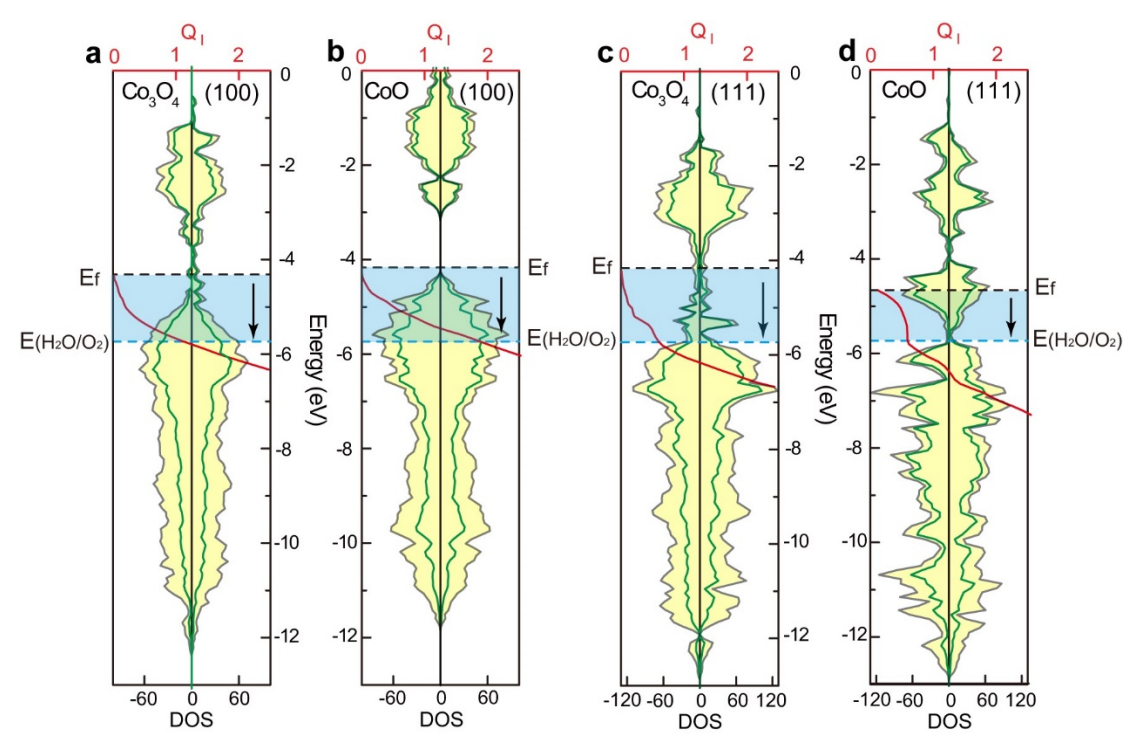
Figure S11. DFT calculation results of (a) Co_3O_4 (100), (b) CoO (100), (c) Co_3O_4 (111), and (d) CoO (111) facets. The total DOS (grey lines) and the PDOS of Co d-orbitals (green lines) are referenced to the vacuum level. The red lines indicate the integral PDOS of Co d-orbitals from the Fermi levels (E_f). The light blue regions from the E_f to the OER potential indicate the PDOS integration ranges to determine the hole storage capacity.

Table S2. The number of Co atoms, Fermi level, and Q_l obtained from DFT calculations for the Co_3O_4 and CoO models with diffrent facets.

	Co_3O_4			CoO		
	Number of Co atoms in model	Fermi level (eV)	Q_l	Number of Co atoms in model	Fermi level (eV)	Q_l
(110)	44	-5.12	0.4	48	-3.95	1.2
(100)	38	-4.31	1.1	48	-4.17	1.9
(111)	60	-4.17	0.6	64	-4.66	0.6

The averaged Q_l values of (110), (100), and (111) facets are 0.7 for Co_3O_4 and 1.2 for CoO, suggesting the larger hole storage capacity of CoO than that of Co_3O_4, which is consistent with the experimental measurements. It is also worth noticing that the reported work functions for bulk Co_3O_4 and bulk CoO by experimental measurements[17] are 6.3 ± 0.3 and 4.6 ± 0.2 eV, respectively, indicating that bulk CoO also has a higher Fermi level than bulk Co_3O_4. That is,

the integration value between the projected DOS of Co d-orbitals from the Fermi level to the OER potential for bulk CoO could be also larger than that for bulk Co_3O_4, which is consistent with our calculation result obtained from the typical facets of Co_3O_4 and CoO.
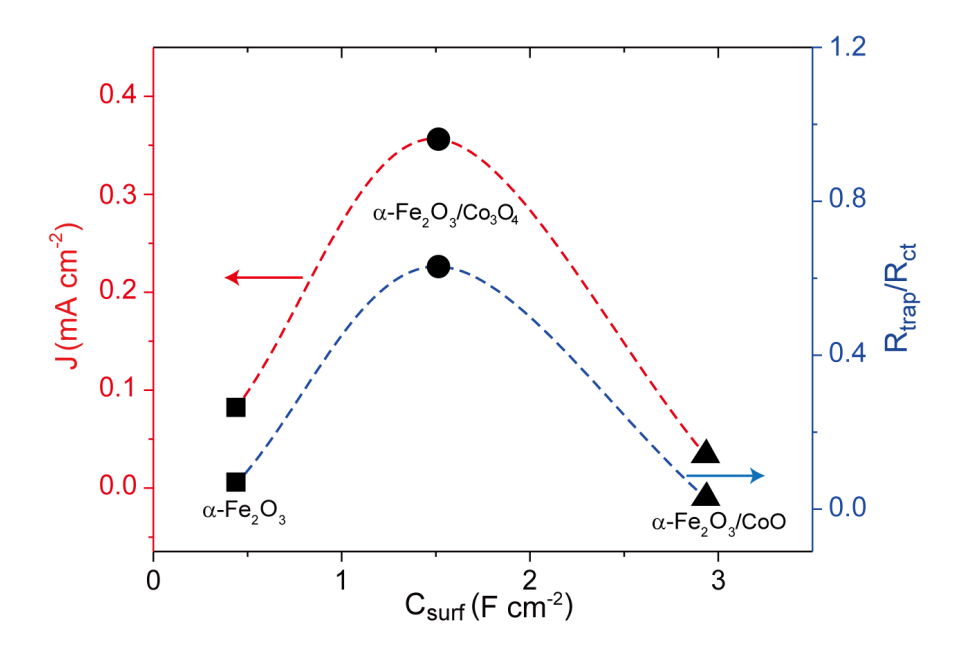
Figure S12. Photocurrent densities and R_{trap}/R_{ct} values as a function surface capacitances. Summarized from α-Fe$_2$O$_3$/Co$_3$O$_4$, α-Fe$_2$O$_3$/CoO, and α-Fe$_2$O$_3$ measured at 1.0 V_{RHE}. Dashed lines are guides to the eye.

The inverted-U-shaped J-C_{surf} curve (red line) shows that the PEC OER activity changes non-monotonically with increasing surface hole density. The R_{trap}/R_{ct}-C_{surf} curve (blue line) also exhibits a consistent inverted-U shape, further revealing that the competition between interfacial charge transfer and recombination determines the photocurrent density, which is controlled by the surface hole density.

References

1. Rivas-Murias, B.; Salgueiriño, V., Thermodynamic CoO-Co$_3$O$_4$ Crossover Using Raman Spectroscopy in Magnetic Octahedron-Shaped Nanocrystals. *J. Raman Spectrosc.* **2017**, *48*, 837-841.

2. Yuan, X.; Ge, H.; Wang, X.; Dong, C.; Dong, W.; Riaz, M. S.; Xu, Z.; Zhang, J.; Huang, F., Controlled Phase Evolution from Co Nanochains to CoO Nanocubes and Their Application as Oer Catalysts. *ACS Energy Lett.* **2017**, *2*, 1208-1213.

3. Guan, J.; Ding, C.; Chen, R.; Huang, B.; Zhang, X.; Fan, F.; Zhang, F.; Li, C., CoO$_x$ Nanoparticle Anchored on Sulfonated-Graphite as Efficient Water Oxidation Catalyst. *Chem. Sci.* **2017**, *8*, 6111-6116.

4. Favaro, M.; Yang, J.; Nappini, S.; Magnano, E.; Toma, F. M.; Crumlin, E. J.; Yano, J.; Sharp, I. D., Understanding the Oxygen Evolution Reaction Mechanism on CoO$_x$ Using Operando Ambient-Pressure X-Ray Photoelectron Spectroscopy. *J. Am. Chem. Soc.* **2017**,

139, 8960-8970.

5. Qiu, J.; Hajibabaei, H.; Nellist, M. R.; Laskowski, F. A.; Hamann, T. W.; Boettcher, S. W., Direct in Situ Measurement of Charge Transfer Processes During Photoelectrochemical Water Oxidation on Catalyzed Hematite. *ACS Central Sci.* **2017**, *3*, 1015-1025.

6. Xu, Y. F.; Wang, X. D.; Chen, H. Y.; Kuang, D. B.; Su, C. Y., Toward High Performance Photoelectrochemical Water Oxidation: Combined Effects of Ultrafine Cobalt Iron Oxide Nanoparticle. *Adv. Func. Mater.* **2016**, *26*, 4414-4421.

7. Varache, R.; Leendertz, C.; Gueunier-Farret, M. E.; Haschke, J.; Muñoz, D.; Korte, L., Investigation of Selective Junctions Using a Newly Developed Tunnel Current Model for Solar Cell Applications. *Sol. Energy Mater. So. Cells* **2015**, *141*, 14-23.

8. Zhang, K.; Dong, T.; Xie, G.; Guan, L.; Guo, B.; Xiang, Q.; Dai, Y.; Tian, L.; Batool, A.; Jan, S. U., Sacrificial Interlayer for Promoting Charge Transport in Hematite Photoanode. *ACS Appl. Mater. Interfaces* **2017**, *9*, 42723-42733.

9. Rao, K. V.; Smakula, A., Dielectric Properties of Cobalt Oxide, Nickel Oxide, and Their Mixed Crystals. *J. Appl. Phys.* **1965**, *36*, 2031-2038.

10. Herner, S. B.; Weerakkody, A. D.; Belkadi, A.; Moddel, G., High Performance Miim Diode Based on Cobalt Oxide/Titanium Oxide. *Appl. Phys. Lett.* **2017**, *110*, 1-34.

11. Lohaus, C.; Klein, A.; Jaegermann, W., Limitation of Fermi Level Shifts by Polaron Defect States in Hematite Photoelectrodes. *Nat. Commun.* **2018**, *9*, 4309.

12. Thorpe, R.; Rangan, S.; Sina, M.; Cosandey, F.; Bartynski, R. A., Conversion Reaction of CoO Polycrystalline Thin Films Exposed to Atomic Lithium. *J. Phys. Chem. C* **2013**, *117*, 14518-14525.

13. Li, C.; Wu, S.; Dong, M.; Shang, A.; Li, X., Optoelectronic Modeling of the $Si/\alpha\text{-}Fe_2O_3$ Heterojunction Photoanode. *Nano Energy* **2017**, *43*, 177-183.

14. Blakemore, J. D.; Gray, H. B.; Winkler, J. R.; Müller, A. M., Co_3O_4 Nanoparticle Water-Oxidation Catalysts Made by Pulsed-Laser Ablation in Liquids. *ACS Catal.* **2013**, *3*, 2497-2500.

15. Daal, H.; Bosman, A., Hall Effect in CoO, NiO, and $\alpha\text{-}Fe_2O_3$. *Phys. Rev.* **1967**, *158*, 736-747.

16. Varghese, B.; Mukherjee, B.; Karthik, K. R. G.; Jinesh, K. B.; Sow, C. H., Electrical and Photoresponse Properties of Co_3O_4 Nanowires. *J. Appl. Phys.* **2012**, *111*, 828-839.

17. Greiner, M. T.; Lu, Z.-H., Thin-Film Metal Oxides in Organic Semiconductor Devices: Their Electronic Structures, Work Functions and Interfaces. *NPG Asia Mater.* **2013**, *5*, e55.